

RESEARCH ARTICLE

10.1029/2018JC014759

Special Section:

The Arctic: An AGU Joint Special Collection

Key Points:

- The 2012-2013 average volume transport of the Atlantic Water boundary current north of Svalbard is 2.08 ± 0.24 Sv
- The transport is maximum in late summer to early fall when the Atlantic Water is warmest and saltiest
- The Atlantic Water layer is ventilated locally via convective overturning in winter and early spring before ice is advected into the region

Correspondence to:

M. D. Pérez-Hernández,
mdolores.perez@whoi.edu

Citation:

Pérez-Hernández, M. D., Pickart, R. S., Torres, D. J., Bahr, F., Sundfjord, A., Ingvaldsen, R., et al. (2019). Structure, transport, and seasonality of the Atlantic Water boundary current north of Svalbard: Results from a yearlong mooring array. *Journal of Geophysical Research: Oceans*, 124, 1679–1698. <https://doi.org/10.1029/2018JC014759>

Received 15 NOV 2018

Accepted 12 FEB 2019

Accepted article online 15 FEB 2019

Published online 14 MAR 2019

Structure, Transport, and Seasonality of the Atlantic Water Boundary Current North of Svalbard: Results From a Yearlong Mooring Array

M. Dolores Pérez-Hernández^{1,2} , Robert S. Pickart¹ , Daniel J. Torres¹ , Frank Bahr¹ , Arild Sundfjord³ , Randi Ingvaldsen⁴ , Angelika H. H. Renner⁴ , Agnieszka Beszczynska-Möller⁵ , Wilken-Jon von Appen⁶ , and Vladimir Pavlov³

¹Department of Physical Oceanography, Woods Hole Oceanographic Institution, Woods Hole, MA, USA, ²Marine and Freshwater Research Institute, Reykjavik, Iceland, ³Norwegian Polar Institute, Tromsø, Norway, ⁴Institute of Marine Research, Tromsø, Norway, ⁵Institute of Oceanology Polish Academy of Sciences, Sopot, Poland, ⁶Alfred Wegener Institute, Helmholtz Centre for Polar and Marine Research, Bremerhaven, Germany

Abstract The characteristics and seasonality of the Svalbard branch of the Atlantic Water (AW) boundary current in the Eurasian Basin are investigated using data from a six-mooring array deployed near 30°E between September 2012 and September 2013. The instrument coverage extended to 1,200-m depth and approximately 50 km offshore of the shelf break, which laterally bracketed the flow. Averaged over the year, the transport of the current over this depth range was 3.96 ± 0.32 Sv ($1 \text{ Sv} = 10^6 \text{ m}^3/\text{s}$). The transport within the AW layer was 2.08 ± 0.24 Sv. The current was typically subsurface intensified, and its dominant variability was associated with pulsing rather than meandering. From late summer to early winter the AW was warmest and saltiest, and its eastward transport was strongest (2.44 ± 0.12 Sv), while from midspring to midsummer the AW was coldest and freshest and its transport was weakest (1.10 ± 0.06 Sv). Deep mixed layers developed through the winter, extending to 400- to 500-m depth in early spring until the pack ice encroached the area from the north shutting off the air-sea buoyancy forcing. This vertical mixing modified a significant portion of the AW layer, suggesting that, as the ice cover continues to decrease in the southern Eurasian Basin, the AW will be more extensively transformed via local ventilation.

Plain Language Summary The Svalbard branch of the Atlantic Water (AW) flows eastward north of Svalbard carrying warm and salty waters along the slope of the western Eurasian Basin. Here we explore the characteristics and seasonality of the boundary current using data from a six-mooring array deployed at 81.7°N, 30.6°E between September 2012 and September 2013. On average the current carries 3.96 ± 0.32 Sv ($1 \text{ Sv} = 10^6 \text{ m}^3/\text{s}$) of which 2.08 ± 0.24 Sv is of AW. From late summer to early winter the AW was warmest and saltiest, and its eastward transport strongest, while from midspring to midsummer the AW was coldest and freshest and its transport weakest. In this region, the layer of AW is modified via convective overturning in winter.

1. Introduction

One of the fundamental aspects of the Arctic Ocean is the circulation and transformation of Atlantic Water (AW), which plays a critical role in Earth's climate system. The modification and conversion AW within the Arctic domain form the headwaters of the global meridional overturning circulation. It is well known that the AW progresses through the Arctic as a system of cyclonic boundary currents (Aagaard & Carmack, 1994; Rudels et al., 2013). However, to date there have been limited direct measurements of the flow, and, as such, there are fundamental aspects of the current that remain unknown. This includes robust quantification of its transport throughout the subbasins of the Arctic, the seasonality of the flow, and the detailed kinematic structure of the boundary current system.

One of the two gateways through which AW enters the Arctic Ocean is Fram Strait, between Greenland and Svalbard. The warm subtropical origin water flows into the strait via the West Spitzbergen Current (WSC). Averaged over the year, the WSC has an average AW temperature of 3.1 ± 0.1 °C and transport of 3.0 ± 0.2 Sv spanning the depth range 0–250 m (Beszczynska-Möller et al., 2012). The flow subsequently bifurcates into what is known as the core WSC (1.3 ± 0.1 Sv) and the offshore WSC (1.7 ± 0.1 Sv) (Beszczynska-Möller et al.,

2012). The core WSC is baroclinically unstable with marked seasonality in temperature, salinity, and stratification (von Appen et al., 2016). It is difficult to detect a seasonal signal in the velocity due to lateral shifts in the location of the current. The offshore WSC, on the other hand, is weaker in summer than in fall/winter Beszczynska-Möller et al. (2012).

Some portion of the offshore WSC recirculates within the strait and flows back to the south as a boundary current over the Greenland slope (Hattermann et al., 2016; Håvik et al., 2017). Ultimately, three branches of AW emerge from the strait and enter the Arctic basin (Figure 1): a branch encircling the Yermak Plateau (the Yermak Plateau Branch; e.g., Meyer, Sundfjord, et al. (2017)), a branch flowing through Yermak Pass (the Yermak Pass branch; Koenig, Provost, Villaceros Robineau, et al., 2017), and a branch following the Svalbard continental slope (the Svalbard branch: Cokelet et al., 2008; Kolås & Fer, 2018; Pérez-Hernández et al., 2017; Våge et al., 2016). Recent model simulations, supported by observations in the Yermak Pass, indicate that the transport is divided predominantly between the Svalbard Branch (annual mean 0.4 Sv) and Yermak Pass Branch (0.9 Sv), with only a minor fraction comprising the Yermak Plateau Branch (0.04 Sv; Koenig, Provost, Sennéchaël, et al., 2017). These numbers imply that all of the offshore WSC recirculates in Fram Strait; however, it must be kept in mind that there is considerable uncertainty in both the measurements and model values.

North of Svalbard, the AW in the Svalbard branch interacts with sea ice, and the resulting melt water isolates it from the sea surface (Ivanov et al., 2009; Onarheim et al., 2014; Polyakov et al., 2011; Renner et al., 2018; Rudels, 2013; Rudels et al., 2014). Using data from a single mooring deployed for 2 years north of Svalbard, Ivanov et al. (2009) provided the first seasonal description of the AW downstream of Fram Strait, determining that the temperature maximum occurs later in the fall than in Fram Strait. This was further documented using more recent data from a mooring located in the same region (Randelhoff et al., 2015). These authors addressed the seasonality of nitrogen and chlorophyll as well, finding that nitrogen concentrations were minimum in summer when primary production peaked due to the onset of ice melt and enhanced stratification. Using data from the same mooring, Renner et al. (2018) determined that, even though advection accounts for 80% of the seasonal heat budget, there is a sizable contribution from local processes such as tidal mixing and air-sea exchange.

Shipboard surveys north of Svalbard have shed light on other aspects of the AW boundary current there (Pérez-Hernández et al., 2017; Våge et al., 2016). The current is 30–40 km wide and covers the approximate depth range of 75–700 m, with a varying kinematic structure. The flow can at times be surface intensified, while other times it is bottom intensified. The current is baroclinically unstable and can meander across the slope. Both anticyclones and cyclones appear to be spawned by the current in this region, the former containing AW in their core. This is consistent with the modeling study of Crews et al. (2018). The mean volume transport of AW computed from a series of shipboard transects occupied in September 2013 was 2.3 ± 0.3 Sv. This agrees with the upstream summer/fall transport estimates of the WSC presented by Koenig, Provost, Villaceros Robineau, et al. (2017) and Beszczynska-Möller et al. (2012) 2.4 and 2.5 Sv, respectively. This implies that the three AW branches emerging from Fram Strait eventually merge with the Svalbard branch north of Svalbard and that there is no recirculation in Fram Strait during summer/fall. Koenig, Provost, Villaceros Robineau, et al. (2017) argue that Yermak Pass branch merges quickly with the Svalbard branch to the east of the pass.

Farther to the east ($\sim 60^\circ\text{E}$ and eastward), the eastward flow of AW is called the “Fram Strait branch”. In the vicinity of Franz Joseph Land, Pnyushkov et al. (2015) found that the maximum AW temperatures occurred in March, while north of the Laptev Sea, Dmitrenko et al. (2006) and Pnyushkov et al. (2015) observed higher/lower temperature and salinity in winter/summer for AW. On the other hand, Pnyushkov et al. (2018) showed higher AW transports in June (~ 9.9 Sv) than in April (~ 0.3 Sv). Dmitrenko et al. (2006) attributed some of the seasonality in the Laptev Sea to lateral shifts of the AW. In particular, the current moved toward the slope in winter and away from the slope in summer. Several studies have documented how the AW advected in the Fram Strait branch mixes with the AW outflow from the Barents Sea via the St. Anna Trough. Above 600-m depth, the mixture is believed to be roughly equal, while deeper than this the AW signature stems mainly from the Barents Sea outflow (Pnyushkov et al., 2018; Schauer et al., 1997). This mixing process makes it more difficult to relate the seasonality of the current east of 70°E to that farther upstream (Dmitrenko et al., 2015; Schauer et al., 1997, 2002).

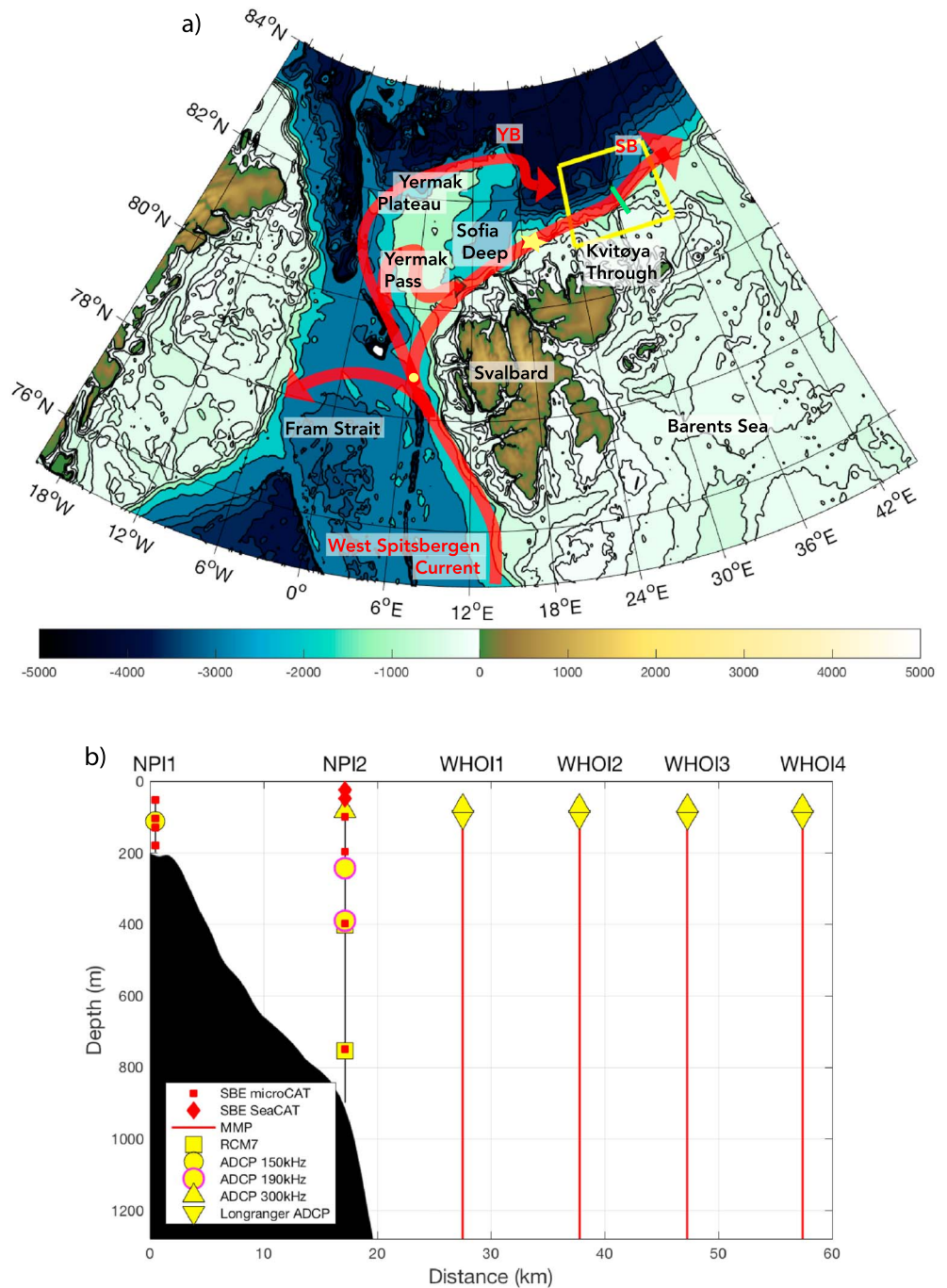


Figure 1. (a) Geographical map of the region where Atlantic Water enters the Arctic Ocean. The schematic circulation of the Atlantic Water is indicated by the red lines. Part of the West Spitsbergen Current recirculates in Fram Strait, and three branches ultimately emerge from the strait: one flows around the Yermak Plateau (YB), one flows through Yermak Pass (YSB), and one flows north of Svalbard (SB). The yellow box indicates the long-term variability and trends in the Atlantic Water inflow region study area; the mooring array is denoted by the green line (see Figure 2 for the individual mooring sites). The yellow dot and star show the position of the additional upstream moorings used in the study: the Fram Strait and Institute of Oceanography, Polish Academy of Sciences mooring. The International Bathymetric Chart of the Arctic Ocean version 3 bathymetry is shaded according to the color bar. (b) Vertical section showing the instrumentation of the array (see the legend). The names of the moorings are indicated along the top. NPI = Norwegian Polar Institute; WHOI = Woods Hole Oceanographic Institution; MMP = McLane Moored Profilers; ADCP = acoustic Doppler current profilers.

Part of the challenge in quantifying the structure and seasonal behavior of the Svalbard branch of the AW is that the mooring measurements to date have been sparse, while shipboard surveys generally occur during the ice-free months of the year. In 2012 the “Long-term variability and trends in the Atlantic Water inflow region” (A-TWAIN) program was initiated to enhance our understanding of the flow of AW north of Svalbard. As part of the program, a high-resolution mooring array was deployed across the current to the base of the continental slope for 1 year near 30°E. This represented the first time that the AW boundary current in the western Eurasian basin was measured with such an extensive array (Figure 1). The goal was to quantify the transport of the current over the full seasonal cycle, determine its kinematic and water mass structure, and address the role of external forcing (e.g., air-sea buoyancy fluxes, wind, and ice) in dictating the variability. The two shoreward-most moorings have already been used to investigate the hydrography and nutrients (Randelhoff et al., 2015) and to quantify the processes controlling the local heat budget in the upper part of the water column (Renner et al., 2018).

Here we present the first results from the full A-TWAIN mooring array deployed northeast of Svalbard from autumn 2012 to autumn 2013. The paper is organized as follows. Section 2 presents the data set and methodology used for the study. Section 3.1 describes the yearlong average structure of the current, and section 3.2 presents the dominant variability in this structure. The seasonal cycle is investigated in section 3.3, which is then related to the seasonality at two upstream locations in section 3.4 to assess the role of advection. In section 3.5 the properties and evolution of the mixed layer are examined and related to driving mechanisms. section 3.6 addresses how the AW layer is modified through the year. The work is summarized in section 4.

2. Data and Methods

2.1. Mooring Measurements

From 24 September 2012 to 15 September 2013 a mooring array was maintained across the Svalbard branch of the AW boundary current, centered at 81.7°N and 30.5°E, as part of the international A-TWAIN project (Figure 1). Eight moorings were deployed, extending from the outer shelf to the deep continental slope. Unfortunately, the mooring situated near the 500-m isobath was lost (presumably due to fishing activity), and the outermost mooring did not return any usable data. Nonetheless, the six remaining moorings provided the first extensive coverage of the boundary current north of Svalbard. The distances between the moorings ranged from approximately 10 to 15 km, which is larger than the local Rossby radius of deformation which is order 8 km (Nurser & Bacon, 2014; Zhao et al., 2014).

The two inshore moorings were provided by the Norwegian Polar Institute (NPI) and the Institute of Marine Research (IMR), while the four offshore most moorings were provided by the Woods Hole Oceanographic Institution (WHOI). The inshore moorings contained Sea-Bird MicroCat and SeaCat conductivity-temperature-depth sensors (CTDs) and two kinds of current measurements: acoustic Doppler current profilers (ADCPs) with a vertical resolution of 4 m (standard deviation of 1.86 cm/s) and Aanderaa Recording Current Meter 7 point current meters (standard deviation of 0.16 cm/s). See Table 1 and Sundfjord et al. (2017) for details. The WHOI moorings consisted of McLane Moored Profilers (MMPs) that sampled the water column between 100-m and 1,250-m depths every 12 hr. Both Sea-Bird and Falmouth Scientific Instrument CTD sensors were used. The vertical profiles had a resolution of 2 m. MicroCats were situated on the top floats and beneath the bottom stops of the profilers, to aid in the calibration of the MMPs. Velocity was measured on the WHOI moorings with an upward facing 300-kHz workhorse ADCP (standard deviation 0.50 cm/s) and a downward facing 75-KHz-Long Ranger ADCP (standard deviation of 1.67 cm/s), with a vertical resolution of 4 and 15 m, respectively (see Table 1). The range of the downward facing ADCPs was approximately 400 m. The velocity records were low passed using a second-order 36-hr Butterworth filter to remove the tidal and inertial signals. The accuracy of each instrument is given in Table 2.

The moored CTD sensors underwent predeployment and postdeployment laboratory calibrations and were further evaluated using shipboard CTD casts (obtained with a Sea-Bird 911+ whose conductivity was calibrated using water samples) from the deployment and recovery cruises (Pérez-Hernández et al., 2017; Våge et al., 2016). The MMP profiles were processed using a set of WHOI-based software routines (available at flotsam.whoi.edu) which involves removing spikes, analyzing sensor lags, and removing density inversions. In addition, the MMPs were calibrated by comparison to Sea-Bird MicroCats located just below the

Table 1
Instruments Contained on Each Mooring Together With Their Sampling Details

Mooring	Instrument	Depth (m)	Starting time	Interval	Ending time
NPI1	SBE37 MicroCat	52	Flooded		
	SBE37 MicroCat	104	16 Sep 2012 17:45	15 min	15 Sep 2013 17:00
	Workhorse 150-kHz ADCP	112	16 Sep 2012 06:45	20 min	15 Sep 2013 10:05
	SBE37 MicroCat	131	16 Sep 2012 17:45	15 min	15 Sep 2013 17:00
	SBE37 MicroCat	180	16 Sep 2012 17:45	15 min	15 Sep 2013 17:00
NPI2	SBE16 SeaCat	25	18 Sep 2012 22:00	15 min	16 Sep 2013 10:15
	SBE16 SeaCat	49	18 Sep 2012 22:00	15 min	06 Sep 2013 23:45
	Workhorse 300-kHz ADCP	84	18 Sep 2012 06:09	20 min	03 Sep 2013 10:09
	SBE37 MicroCat	101	18 Sep 2012 12:30	15 min	16 Sep 2013 12:30
	SBE37 MicroCat	198	18 Sep 2012 12:30	15 min	16 Sep 2013 10:15
	ADCP 190 kHz	244	20 Sep 2012 10:10	20 min	16 Sep 2013 13:50
	ADCP 190 kHz	390	Failed		
	SBE37 MicroCat	399	18 Sep 2012 12:30	15 min	16 Sep 2013 10:15
	RCM7	402	18 Sep 2012 14:00	1 hr	16 Sep 2013 09:00
	SBE37 MicroCat	751	18 Sep 2012 12:30	15 min	16 Sep 2013 10:15
	RCM7	754	18 Sep 2012 14:00	1 hr	16 Sep 2013 09:00
WHOI1	Workhorse 300-kHz ADCP	50	13 Sep 2012 12:00	1 hr	30 Aug 2013 22:00
	Long Ranger 75-kHz ADCP	53	13 Sep 2012 12:00	1 hr	17 Sep 2013 09:00
	MMP	60–1,280	24 Sep 2012 00:28	12 hr	16 Sep 2013 12:41
WHOI2	Workhorse 300-kHz ADCP	50	19 Sep 2012 12:00	1 hr	15 Sep 2013 09:00
	Long Ranger 75-kHz ADCP	53	13 Sep 2012 12:00	1 hr	17 Sep 2013 17:00
	MMP	60–1,280	24 Sep 2012 00:33	12 hr	17 Sep 2013 00:49
WHOI3	Workhorse 300-kHz ADCP	50	14 Sep 2012 05:00	1 hr	1 Sep 2013 10:00
	Long Ranger 75-kHz ADCP	53	13 Sep 2012 12:00	1 hr	9 Aug 2013 00:00
	MMP	60–1,280	24 Sep 2012 00:00	12 hr	18 Sep 2013 12:12
WHOI4	Workhorse 300-kHz ADCP	50	13 Sep 2012 12:00	1 hr	19 Sep 2013 18:00
	Long Ranger 75-kHz ADCP	53	13 Sep 2012 12:00	1 hr	12 Sep 2013 06:00
	MMP	60–1,280	24 Sep 2012 00:39	12 hr	19 Sep 2013 00:02

Note. The third column shows the depth of the instrument; for the MicroCats the depth shown is the average depth measured. Time is Coordinated Universal Time (UTC). The “NPI1” and “NPI2” are called “A200” and “A800” in Renner et al. (2018). NPI = Norwegian Polar Institute; ADCP = acoustic Doppler current profilers; WHOI = Woods Hole Oceanographic Institution; MMP = McLane Moored Profilers.

MMP bottom stop. The conductivity sensor on the WHOI3 MMP failed at the start of the deployment period. We created a synthesized salinity record at this site based on the temperature/salinity relationship at the two bounding moorings.

Vertical sections of potential temperature (θ), salinity (S), and potential density (σ_θ) were created using Laplacian-spline interpolation with a grid spacing of 10 km in cross-stream distance (x) and 60 m in depth (z) for every time step. Because the ADCP measurements on the continental slope only reached ~500-m depth, we constructed vertical sections of absolute geostrophic velocity in order to extend the coverage to the full depth range of the MMPs. These sections were computed following the methodology of Fratantoni et al. (2001). For each individual section, the boundary current was defined for that time step

Table 2
Instrument's Accuracy

Instrument	Conductivity	Temperature	Velocity
SBE37 MicroCat	± 0.0003 S/m	± 0.002 °C (–5 to 35 °C)	
SBE16 SeaCat	± 0.001 S/m	± 0.01 °C	
ADCP 150 kHz			1% of measured value
ADCP 190 kHz			1% of measured value
Long Ranger 75 kHz ADCP			$\pm 1\% \pm 5$ mm/s
Workhorse 300 kHz ADCP			0.5% of the water velocity relative to ADCP ± 0.5 cm/s, 0.1 cm/s ± 5 m/s (default), and ± 20 m/s (max) 1–255
MMP (SBE37 MicroCat)	± 0.0003 S/m	± 0.002 °C (–5 to 35 °C);	
RCM7	$\pm 0.1\%$ of range.	± 0.05 °C	± 1 cm/s or $\pm 4\%$ of actual speed whichever is greater

Note. ADCP = acoustic Doppler current profilers; MMP = McLane Moored Profilers.

as the area where the velocity was $>10\%$ of the maximum velocity in the section. This definition was altered when features such as eddies were clearly present offshore of the boundary current. The AW portion of the boundary current was determined in the same manner as was done in Pérez-Hernández et al. (2017). In particular, AW is defined as $\theta \geq 1$ °C, $S \geq 34.9$, and $\sigma_\theta \geq 27.6$ kg/m³. Transport errors are expressed as standard deviations.

We also make use of data from a single mooring maintained by the Institute of Oceanology, Polish Academy of Sciences (IOPAN) that was positioned north of Svalbard approximately 140 km to the west of the A-TWAIN array during the same year (see Figure 1a for the location of the IOPAN mooring). The mooring was situated at the 800-m isobath and contained an MMP that profiled the water column between 50 and 750 m every 12 hr. The CTD data were calibrated and processed in similar fashion to the A-TWAIN data (see Renner et al., 2018).

We also compare our results with Fram Strait using data from a MicroCat situated on the F3-15 mooring located at 78.831°N, 8.005°E in a water depth of 1,010 m. The MicroCat nominally resided at 57-m depth. However, due to severe mooring blowdowns, the instrument on average was at 117-m depth (von Appen et al., 2015). Hence, the MicroCat measures the warmer (shallower) part of the AW layer in the WSC.

2.2. Reanalysis Data

To document the regional wind field during the study period, we use the ERA-Interim daily global atmospheric reanalysis product. The data were downloaded from the European Centre for Medium Range Weather Forecast public data sets (<http://apps.ecmwf.int/datasets/>). The spatial resolution is 0.75°, and the temporal resolution is 12 hr (Dee et al., 2011).

2.3. Sea Ice Concentration Data

The MASAM2 (MASAM2 is an acronym created from 2 two acronyms: The MASIE-AMSR2 (MASAM2) daily 4-km sea ice concentration is a prototype concentration product that is a blend of two other daily sea ice data products: ice coverage from the Multisensor Analyzed Sea Ice Extent [MASIE] product at a 4-km grid cell size and ice concentration from the Advanced Microwave Scanning Radiometer 2 [AMSR2].) sea ice concentration (Fetterer et al., 2015) was downloaded from the National Snow and Ice Data Center (<https://nsidc.org/data/docs/noaa/g10005-masam2/>). This sea ice product has a 4-km resolution and blends sea ice extent from the Multisensor Analyzed Sea Ice Extent product and sea ice concentration from the Advanced Microwave Scanning Radiometer 2. This product is more accurate than using Advanced Microwave Scanning Radiometer 2 alone as it uses microwave and infrared measurements (see <http://nsidc.org/data/G10005>).

2.4. Mixed-Layer Analysis

Properties of the mixed layer were analyzed using the MMP data from the WHOI and IOPOAN moorings, which had top floats at depths of 100 and 50 m, respectively. Therefore, we could only document the periods when the mixed layers exceeded these depths. At each time step, the depth of the mixed layer was determined following the method of Pickart et al. (2002). This involves making an initial estimate visually, then computing a two-standard deviation envelope over this portion of the profile. The mixed-layer depth (MLD) is then determined objectively as the depth where the profile passes out of this envelope. A linear fit is then made to the mixed-layer profile for θ , S , and σ_θ , the average of which is taken to be the value of the mixed layer for the variable in question. For mooring WHOI3, where the salinity (and hence density) profiles were determined synthetically, we used the temperature profiles to determine the MLDs.

One-dimensional mixed-layer modeling was carried out using the model of Price et al. (1986). The model is forced using the ERA-Interim data and initialized with the 0600 3 November 2012 profiles of θ , S , and σ_θ from the WHOI1 mooring. This is the first time that the mixed layer at the site extended deeper than 100 m (the upper measurement limit of the MMP). The hydrographic profiles were extrapolated to the sea surface. As time progresses, if the density profile becomes unstable, the model mixes the water column until it attains static stability (increasing density gradient), mixing layer stability (bulk Richardson number), and shear flow stability (gradient Richardson number). Sensitivity tests were run where the model was forced either with wind stress, heat flux, freshwater flux, or different combinations of these. The effects of the wind and freshwater forcing were found to be negligible; hence, the model was forced with heat flux only.

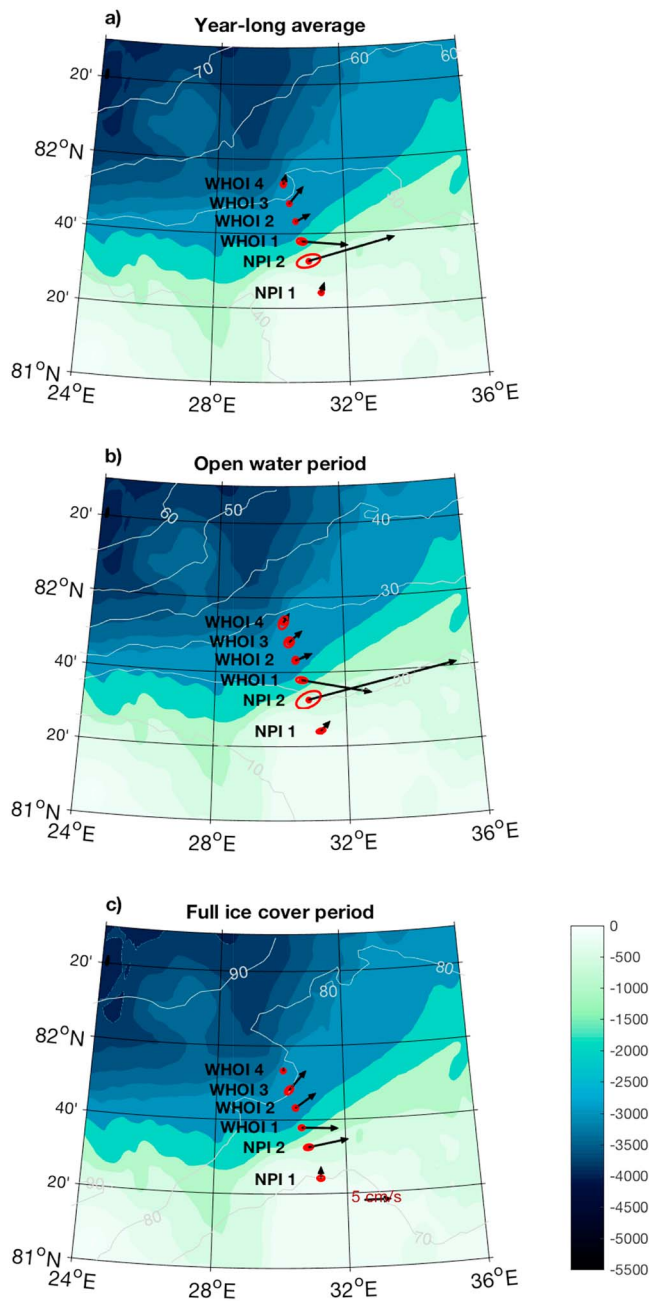


Figure 2. Vertically averaged velocities at the mooring sites together with their standard ellipses for three time periods: (a) yearlong average, (b) open water period, and (c) full ice cover period. The average sea ice concentration for each time period is shown by the white contours. The IBCAO version 3 bathymetry is shaded according to the color bar. WHOI = Woods Hole Oceanographic Institution; NPI = Norwegian Polar Institute.

3. Results

3.1. Yearlong Average

The yearlong mean flow vectors (from the ADCPs), averaged over the full water column, show that the boundary current is strongest on the upper continental slope (Figure 2a). Progressing offshore, the current weakens and the vectors rotate to the northeast, generally following the topography. (It is unclear why the WHOI-1 vector is directed eastward and hence onshore; this could be due to small-scale variations of the bathymetry not captured in the IBCAO v3 data set.) The standard error ellipses are included in Figure 2, indicating that the mean flow is statistically significant everywhere (the average integral time scale across the array was 5.7 days). It is clear that, in the mean, the array bracketed the boundary current: the flow at the offshore-most mooring WHOI4 is weak, as is the flow at the inshore-most mooring NPI1, which is directed off the shelf.

Averaged over the year, the wind speed at the array site was 6.7 m/s from the southeast, while the ice cover ranged from 45% on the shelf to 55% at the offshore mooring location (Figure 3a). The mean vertical sections for the yearlong deployment are shown in Figures 3b–3d, where we have indicated the location of the AW layer (bounded by the dashed lines in the figure). As noted above we adopted the same definition for AW that was used in Pérez-Hernández et al. (2017); namely, AW corresponds to $\theta \geq 1$ °C, $S \geq 34.9$, and $\sigma_\theta \geq 27.6$ kg/m³. One sees that the AW layer roughly spans the depth range 150–600 m and that the temperature maximum is shallower and displaced farther offshore than the salinity maximum. Above the AW layer, Polar Surface warm Water (PSWw) can be found at times with lower salinities than AW. Below the AW layer is Arctic Intermediate Water (AIW; see also Pérez-Hernández et al., 2017).

The vertical section of averaged absolute geostrophic velocity shows eastward flow across the entire array, with a core value of ~17 cm/s near the continental slope (Figure 3d). The maximum flow likely would have been measured at the 500-m isobath mooring, which was lost. Based on various testing, we chose the grid spacing and interpolation parameters in a way to limit any unrealistic extrapolation in this region of missing data. The mean core velocity is similar to other reported synoptic estimates in the literature (e.g., Meyer, Sundfjord, et al., 2017; Pnyushkov et al., 2015; Schauer et al., 2002, 2004). Based on our criterion of 10% of the core absolute geostrophic velocity to define the outer edge of the current, the array bracketed the entire current in the mean (i.e., the 10% contour is inshore of mooring WHOI4). The mean current is subsurface intensified, corresponding to the upward sloping isopycnals toward the coast in the upper layer and a slight downward tilt of the deep isopycnals (recall that the section displays absolute geostrophic velocity). It should be noted that previous shipboard realizations of the current implied that it was just as apt to be surface intensified (Våge et al., 2016; Pérez-Hernández et al. (2017), which is not supported by the yearlong mooring data. Offshore of the core, the flow is mainly barotropic. The e -folding width of the current is 67.5 km.

Based on the mean section, the transport of the boundary current at this location is 3.96 ± 0.32 Sv to the east of which 2.08 ± 0.24 Sv is AW, 0.99 ± 0.18 Sv is AIW, and 0.26 ± 0.12 Sv is PSWw (Table 3). This value of AW transport is in line with the reported synoptic estimates from the deployment and recovery cruises of the array, 1.8 ± 0.3 and 2.31 ± 0.29 Sv (Pérez-Hernández et al., 2017; Våge et al., 2016), respectively. While

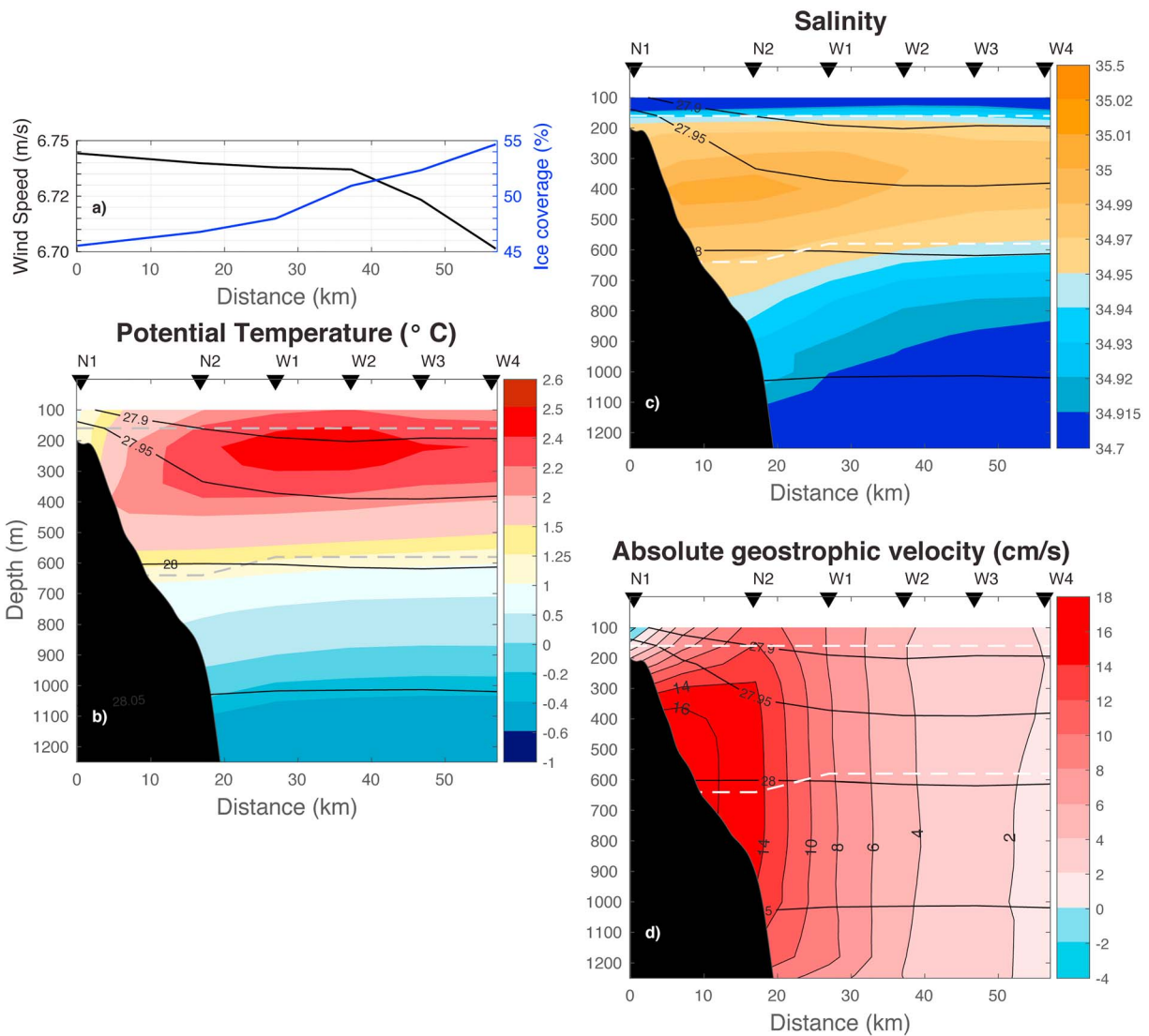


Figure 3. (a) Yearlong averaged wind speed (left axis) and percent sea ice coverage (right axis). (b–d) Yearlong averaged vertical sections of potential temperature, salinity, and absolute geostrophic velocity (color). The average potential density is shown by the black contours. The gray contours in (d) correspond to 1-cm/s increments in velocity. The dashed lines denote the boundaries of the Atlantic Water layer. The triangles along the top of the sections labeled N and W indicate the Norwegian Polar Institute and Woods Hole Oceanographic Institution moorings, respectively. The 10% value of the core velocity lies near the 2-cm/s isoline.

there is also agreement in the transport of PSWw between the mooring array and the shipboard surveys, the same is not true for the AIW simply because the depth range of the mooring data exceeds that of the shipboard measurements.

Table 3

Average Eastward Volume Transports for the Different Water Masses: Year-Round Average (Second Column) and for the Different Ice Seasons (Last Two Columns)

Water mass	Average	Open water	Full ice cover
AW	2.08 ± 0.24	2.44 ± 0.12	1.10 ± 0.06
PSWw	0.26 ± 0.12	0.32 ± 0.00	0.27 ± 0.00
AIW	0.99 ± 0.18	0.46 ± 0.07	0.88 ± 0.05
Total	3.96 ± 0.32	3.30 ± 0.13	2.32 ± 0.06

Note. AW = Atlantic water; PSWw = warm polar surface water; AIW = Arctic intermediate water.

The AW volume transport reported here is the first yearlong mean estimate based on a mooring array in the western Nansen Basin that resolves and brackets the current. It is therefore of interest to compare our value with the mooring-based yearlong mean estimate in Fram Strait. As noted in section 1, Beszczynska-Möller et al. (2012) computed an average AW (defined as $>2^\circ\text{C}$) northward transport in Fram Strait of 3.0 ± 0.2 Sv (1.3 ± 0.1 Sv in the core WSC and 1.7 ± 0.1 Sv in the offshore WSC), compared to our yearlong mean value of 2.08 ± 0.24 Sv near 30°E . This difference suggests two possibilities: (1) Roughly 1 Sv of the offshore WSC recirculates in Fram Strait and all of the remaining transport ends up in the Svalbard branch by the longitude of the A-TWAIN site, which

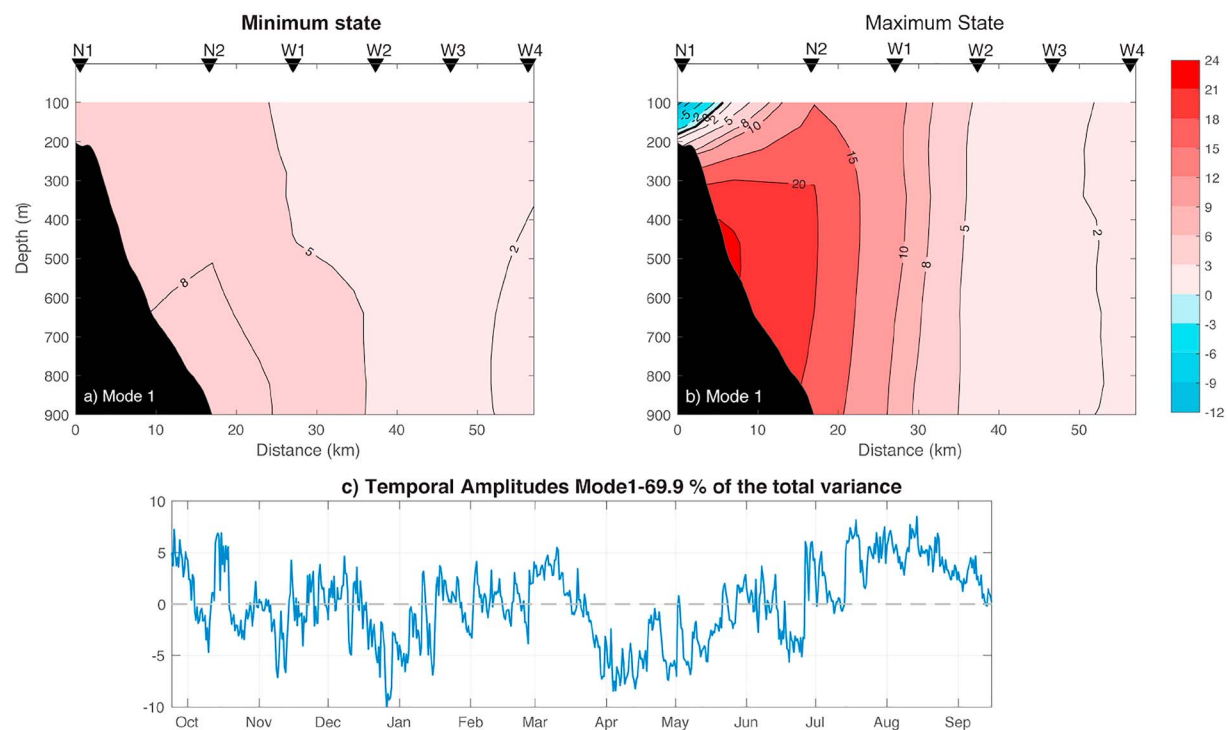


Figure 4. (a, b) The two extreme states of the boundary current associated with empirical orthogonal function mode 1, determined by adding the maximum/minimum values of the mode into the mean vertical section of absolute geostrophic velocity. The triangles along the top of the sections labeled N and W indicate the Norwegian Polar Institute and Woods Hole Oceanographic Institution moorings, respectively. (c) The temporal amplitude of the mode.

implies that the Yermak Plateau and Yermak Pass branches merge quickly with the Svalbard branch. This is consistent with the results of Koenig, Provost, Villaciers Robineau, et al. (2017). (2) Less of the offshore WSC recirculates in Fram Strait, which implies that not all of the Yermak Plateau and Yermak Pass branches have joined the Svalbard branch by the location of our array. Regardless of which scenario applies, we stress that it is very difficult to identify the AW in a consistent fashion between the A-TWAIN site and Fram Strait due to the transformation of the water via ocean-ice-atmosphere interaction and mixing as it advects eastward (Meyer, Fer, et al., 2017; Onarheim et al., 2014; Pérez-Hernández et al., 2017; Rudels et al., 2014). Also, Crews et al. (2018) estimate that around 10% of the AW is lost from the boundary current north of Svalbard to anticyclonic eddies. Hence, even though both Beszczynska-Möller et al. (2012) and our study define AW in an objective manner, it is hard to make a precise comparison.

3.2. Structural Variability

To assess the variability of the current, an empirical orthogonal function analysis was carried out using the absolute geostrophic velocity sections. A dominant mode emerged, accounting for nearly 70% of the overall variance, which corresponds to a pulsing of the boundary current. This is visualized by adding the maximum/minimum values of the mode into the mean section (Figures 4a and 4b). In the maximum state, the core of the current is nearly 3 times stronger than the minimum state. In both states, the current is bottom intensified. When the boundary current is stronger, a counter flow (to the west) develops over the outer shelf. The principle component time series for mode 1 shows that the current was strongest from mid-July to mid-August (Figure 4c).

The shipboard sections presented in Pérez-Hernández et al. (2017), occupied over a 2-week period while the mooring array was being recovered in September 2013, showed the boundary current in a surface-intensified state. Furthermore, the sections revealed that the current can meander across the slope. While the mooring data indicate that this scenario does occur at times, it is much more common for the boundary current to be bottom intensified and to vary in strength rather than in cross-slope position.

3.3. Seasonality

During the yearlong deployment of the array, the wind was quite variable with no preferred direction (Figure 5a). This is due to the large number of storms that propagate through this region (Bengtsson et al., 2006). The strongest wind speeds occurred between mid-December 2012 and mid-January 2013, reaching up to 20 m/s (Figure 5b). Over the course of the year there were three general ice regimes: nearly open water (average concentration of 5%) from early-September to mid-December (this period included two calendar years), partial ice concentration from mid-December to early-April and again from early-August to early-September, and consolidated ice cover from early-April to early-August (i.e., in between the two partial ice periods; Figure 5c).

The properties and strength of the boundary current varied in accordance with these ice regimes. The mean depth-averaged vectors for the open water and full-ice cover periods are shown in Figures 2b and 2c, respectively. This reveals that the core of the boundary current was stronger when there was no ice. The time series in Figure 5d also show that the current was warmest, saltiest, and had the largest volume transport during the open water period, while during the time of partial ice cover following the open water period it cooled, freshened, and decreased in transport. When the region was nearly fully ice covered, the current remained relatively cold, fresh, and weak. Note that, starting in early February after the sharp transition in boundary current properties, the current continued to cool slightly until the early summer but became systematically saltier over this period. Not until the partial ice period in August did the pronounced warming and salinification commence.

To further explore this seasonality, we constructed composite average vertical sections of different properties for the open water period versus the full ice cover period (Figure 6). In the former, the AW is warmest and saltiest over the upper slope, spanning a depth range from nearly 600 m to the top of our data coverage at 100 m (Using data from the NPI moorings only, which have instruments shallower than the WHOI moorings, Renner et al., 2018, showed that the AW at times reached as shallow as 25 m). A region of enhanced stratification extends over much of the layer. The total volume transport of the boundary current is 3.30 ± 0.13 Sv of which 2.44 ± 0.12 Sv is AW (Table 3). By contrast, when the ice cover is heavily consolidated, the property core of the AW is located farther offshore and the layer is considerably thinner over the upper slope. The stratification is significantly weaker as well. The total eastward transport of the boundary current is 2.32 ± 0.06 Sv of which 1.10 ± 0.06 Sv is AW (Table 3). Hence, going from the open water period to the time of nearly complete ice cover, the AW core on average becomes 0.84 °C colder, 0.034 fresher, and its volume transport diminishes by 1.34 Sv.

The waters bounding the AW also exhibit changes between these two seasons. The fresh upper layer of PSWw, barely present during the open water period, expands during the full ice cover period to nearly 200-m depth. However, the velocity of the PSWw is smaller during this time period so that, despite the increase in cross-sectional area, the volume flux remains approximately the same at 0.30 ± 0.01 Sv (Table 3). Note that in the vicinity of the shelf break the water becomes markedly colder and fresher, and the velocity reverses. This suggests that, at this time of year, the flow on the shelf is westward transporting a distinct water mass, perhaps melt water. Beneath the AW layer the properties of the AIW also vary. In particular, the average temperature and salinity of the layer changes by 0.06 °C and -0.014 , respectively, during the later period (when the AW is warmer and fresher). At the same time, the transport of the AIW layer approximately doubles from 0.46 ± 0.07 to 0.88 ± 0.05 Sv (Table 3). Overall, across the entire section (i.e., to a depth of 1,250 m), the AW accounts for 60% of the seasonal amplitude.

3.4. Contribution From Upstream

To get a deeper understanding of the seasonal cycle of AW, Figure 7 compares the characteristics of the Svalbard Branch against that measured at two upstream locations—in Fram Strait at the 117-m depth MicroCat of mooring F3-15 (see von Appen et al., 2016) and with the IOPAN mooring located 140 km to the west of the A-TWAIN array (see Figure 1). Note that with the profiling instruments at the IOPAN and WHOI moorings the average temperature of the AW layer can be calculated, while this is not possible for the point measurement in Fram Strait.

Comparison of the temperature time series between the AW at the A-TWAIN site and Fram Strait reveals a clear 2-month lag, with Fram Strait leading (Figure 7, where we have shifted the x axis between the two sites

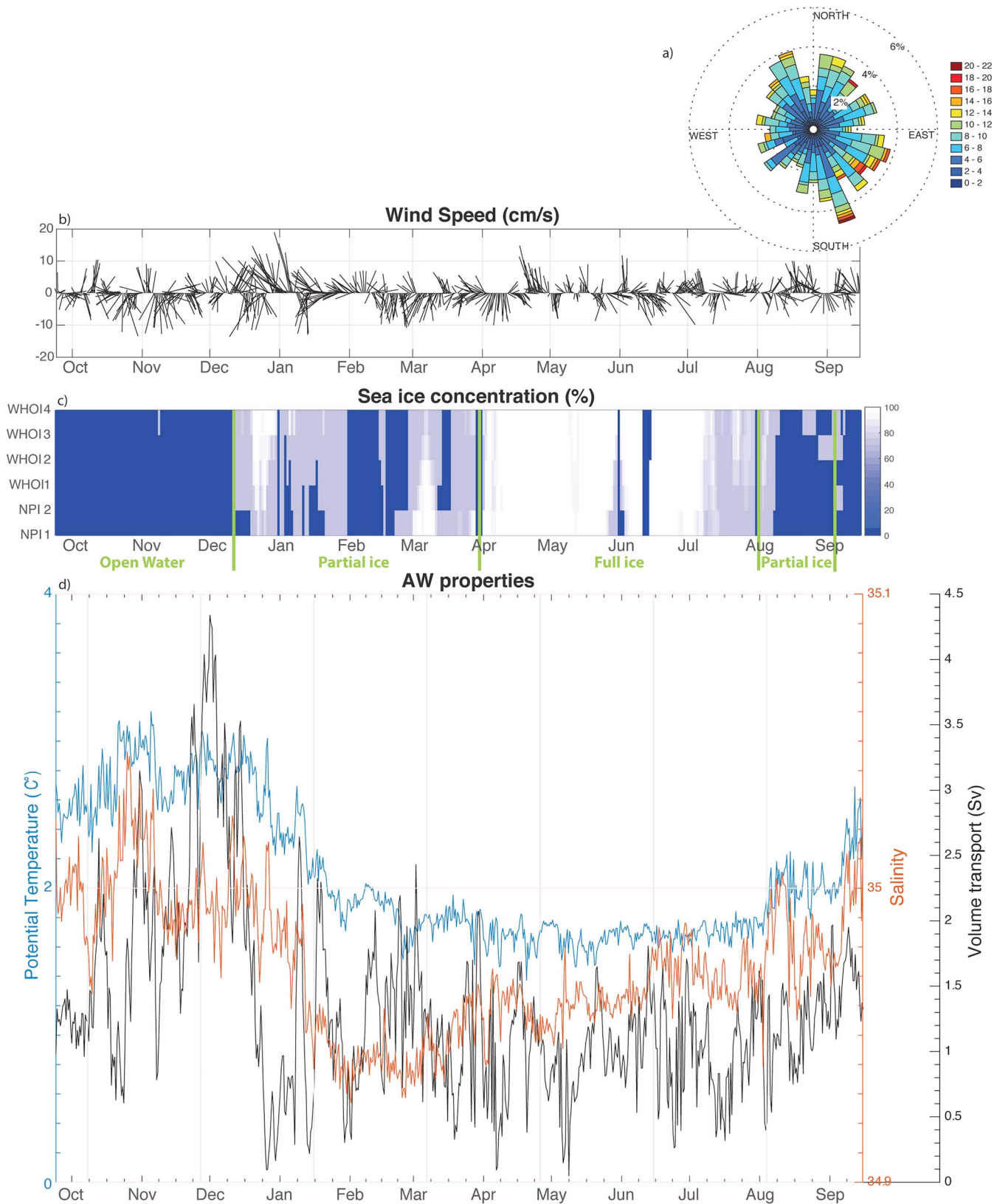


Figure 5. (a) Wind rose and (b) time series of wind vectors, calculated using the Era-Interim reanalysis data. (c) MASAM2 sea ice concentration across the mooring array. The green lines mark the different ice regimes discussed in the text. (d) Average temperature (blue curve), salinity (red curve), and volume transport (black curve) of the AW layer in the boundary current. WHOI = Woods Hole Oceanographic Institution; NPI = Norwegian Polar Institute; AW = Atlantic Water.

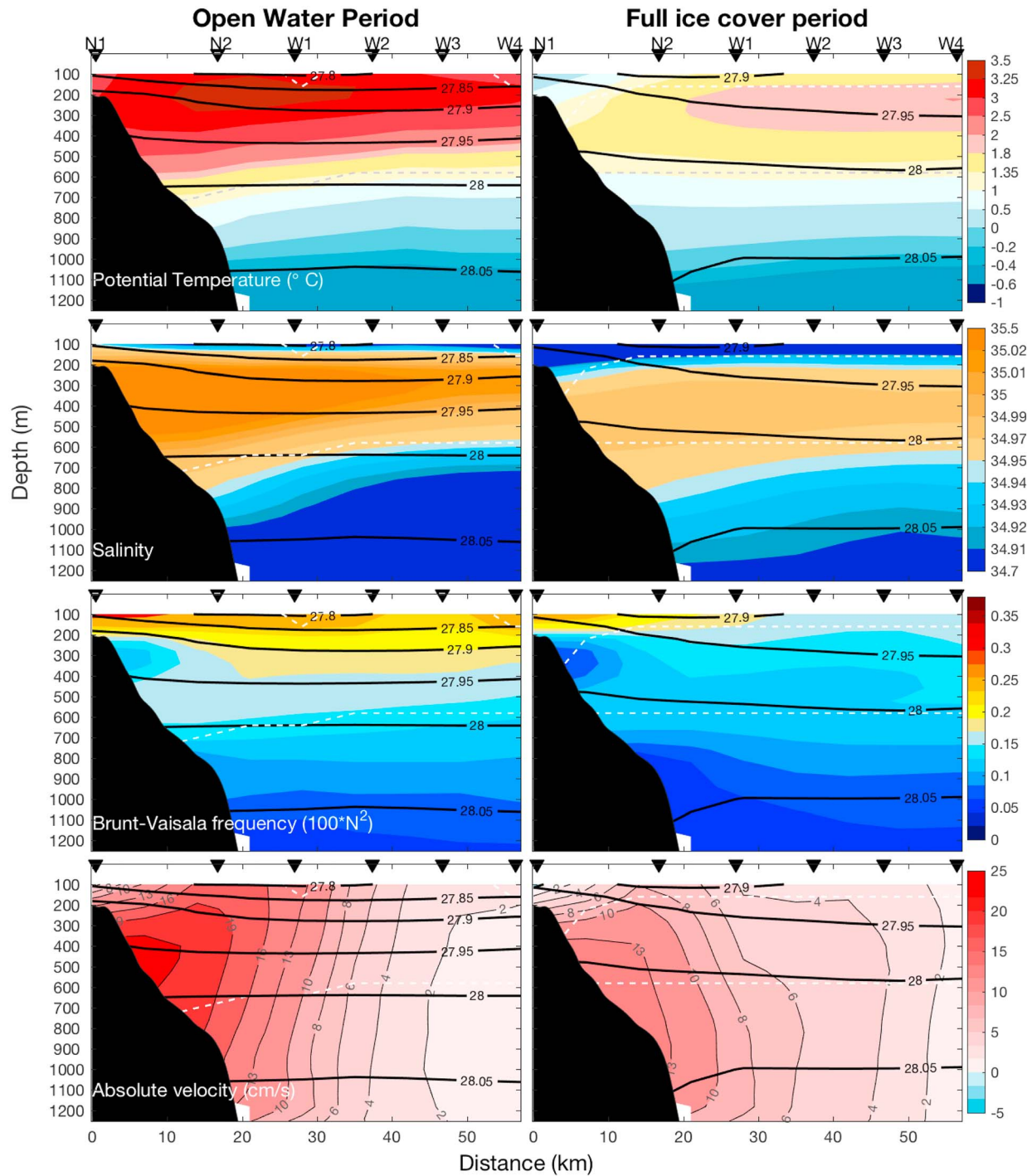


Figure 6. Composite vertical sections of potential temperature (first row), salinity (second row), Brunt-Väisälä frequency (third row), and absolute geostrophic velocity (fourth row) for the open water (left column) and full ice cover (right column) periods discussed in the text. The white dashed lines denote the boundaries of the Atlantic Water layer. The triangles along the top of the sections labeled N and W indicate the Norwegian Polar Institute and Woods Hole Oceanographic Institution moorings, respectively.

accordingly). This is consistent with the measured advective speeds of 16–18 cm/s at the Fram Strait location and the A-TWAIN site. Such an advective velocity implies a lag of 40–70 days depending on whether a parcel follows the slope route or the Yermak Pass route as suggested in Koenig et al. (2017). The lag between the IOPAN mooring and the A-TWAIN site is approximately 5 days (see also Renner et al., 2018). Curiously,

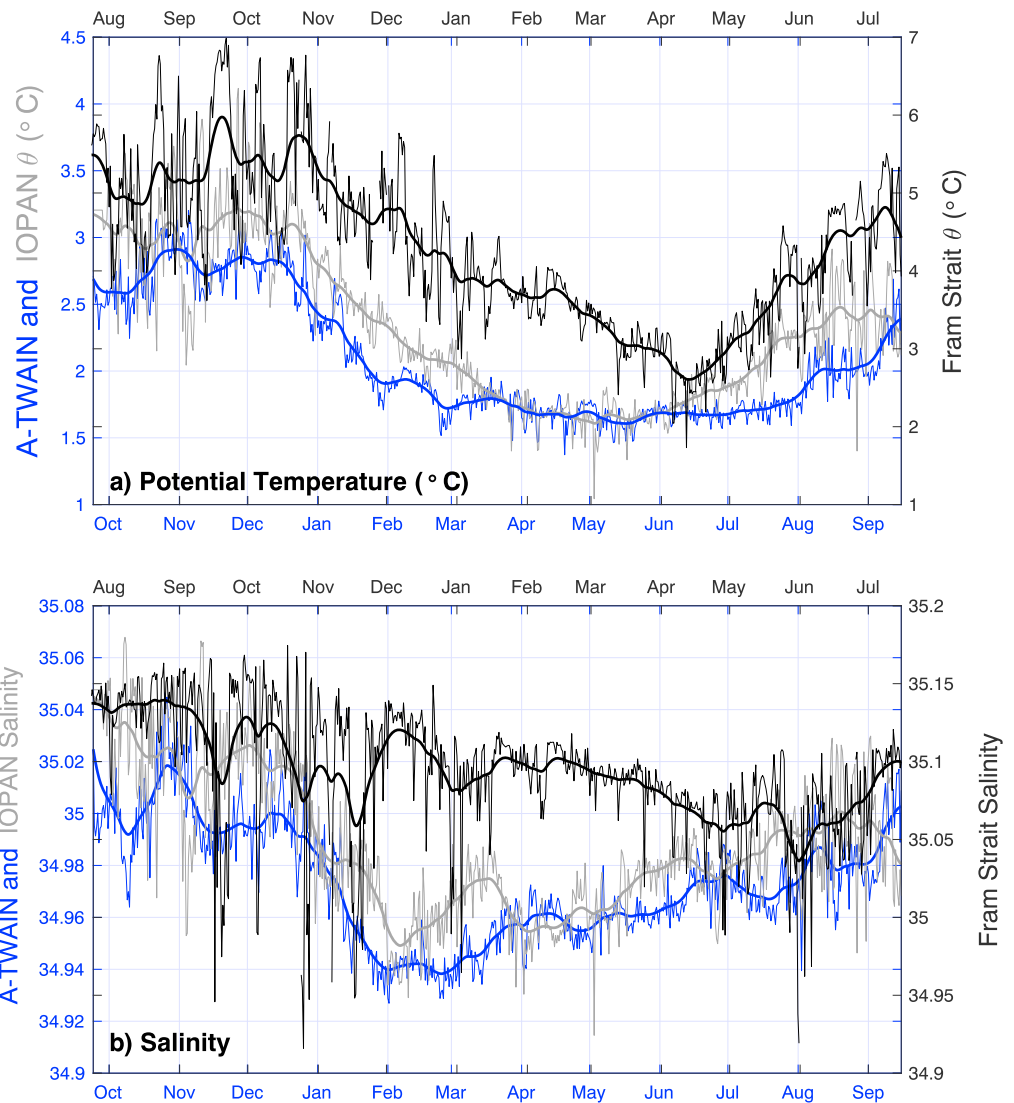


Figure 7. Time series of (a) potential temperature and (b) salinity for the Atlantic Water layer measured at the A-TWAIN study site (blue) and the IOPAN mooring (gray). The Atlantic Water temperature at 117 m in Fram Strait is shown in black. The Fram Strait time series has been lagged by 2 months relative to the other two time series. A-TWAIN = Long-term variability and trends in the Atlantic Water inflow region; IOPAN = Institute of Oceanology, Polish Academy of Sciences.

while the AW temperatures at Fram Strait and north of Svalbard display a very similar pattern (correlation of 0.7 and 0.8 for Fram Strait and IOPAN, respectively, Figure 7a), salinity does not show such a clear relationship between the Svalbard slope and Fram Strait (there is no significant correlation; Figure 7b). This suggests that there may be local processes on the slope that affect the salinity more than the temperature. We now explore the local modification of the water column at the A-TWAIN and IOPAN sites via convective overturning driven by air-sea fluxes.

3.5. MLDs

MLDs were estimated following the methodology of Pickart et al. (2002) for the A-TWAIN array (for the moorings that employed CTD profilers) and for the IOPAN profiling mooring. Figure 8a shows a representative mixed layer at each site, and Figure 8b compares the time series of MLD between the IOPAN mooring and the WHOI1 mooring (the shallowest of the WHOI moorings, which is closest in bottom depth to the IOPAN site). We note that the top float of the IOPAN mooring was at 50-m depth versus 100-m depth for

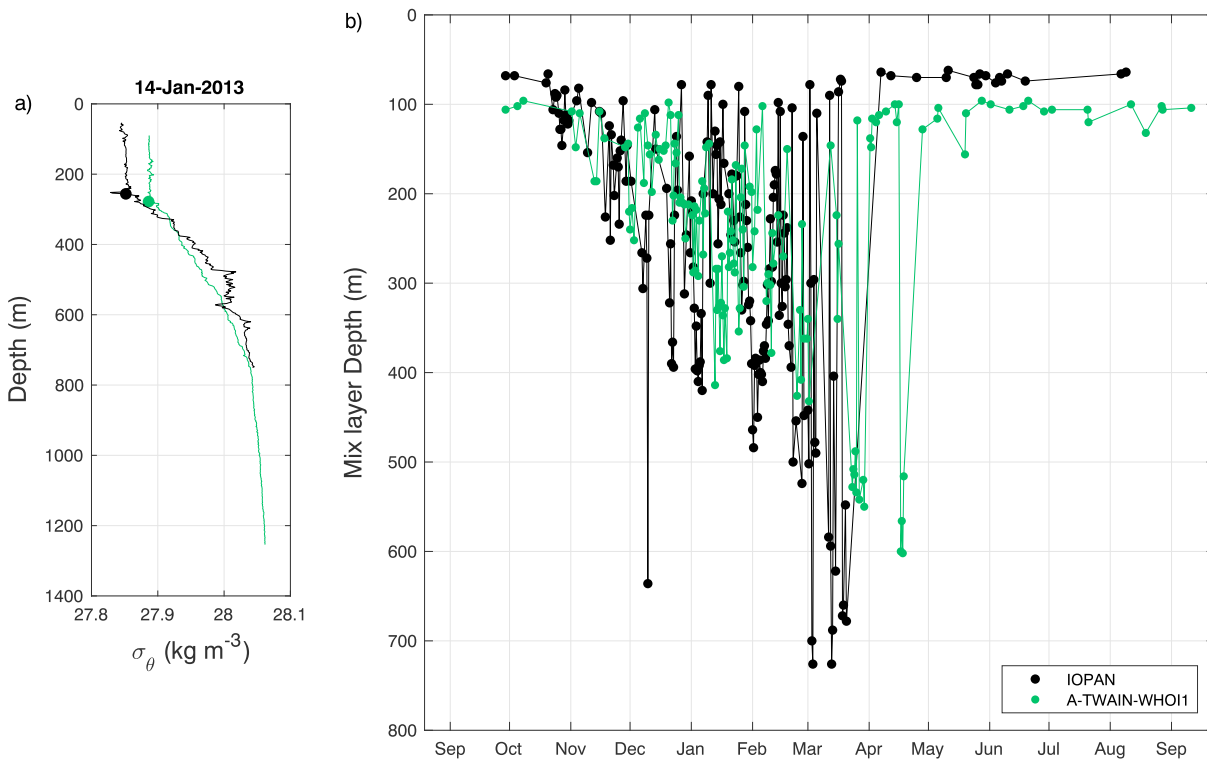


Figure 8. (a) Representative density profiles in January 2013 from the WHOI-1 mooring (green) and the IOPAN mooring (black), where the depth of the mixed layer is indicated by the dot. (b) Time series of mixed-layer depth at the WHOI-1 mooring (green dots) and the IOPAN mooring (black dots). IOPAN = Institute of Oceanology, Polish Academy of Sciences; A-TWAIN = Long-term variability and trends in the Atlantic Water inflow region; WHOI = Woods Hole Oceanographic Institution.

the WHOI moorings. One sees that there is generally good agreement between the two locations (separated by 140 km): the mixed layers steadily deepened from early-November until early-April when they abruptly became shallow (if a mixed layer was not observed at a given time step, then no symbol was plotted). The transition to shallow MLDs corresponded to the onset of full ice cover in early-April (Figure 5b). This implies that the ice was not locally formed; otherwise, brine-driven convection would have deepened the mixed layer further (plus there was no evidence of salinification of the mixed layer at this time; see below). Randelhoff et al. (2015) observed in the data set of the NPI2 mooring that the stratification breaks down in December and the MLD deepens, mixing near-surface cold and fresh water with the AW. Meyer, Sundfjord, et al. (2017) noted deeper MLDs in March versus June from drifting ice camps deployed north of Svalbard. However, the deepest MLD recorded by Meyer, Sundfjord, et al. (2017) was only 100 m. To our knowledge, this is the first time that deep MLDs (exceeding 500 m) have been observed on the continental slope of the Nansen Basin.

Are these measured MLDs consistent with the atmospheric forcing? To assess this, we used the one-dimensional mixing model of Price et al. (1986; hereafter referred to as the PWP model). The model was initialized with the 06:00 UTC 3 November 2012 profile of temperature, salinity, and density from the WHOI1 mooring and forced with the ERA-Interim reanalysis heat flux time series for the grid point closest to the mooring. The initial hydrographic profile chosen was the first one of the year with a MLD that significantly exceeded the depth of the mooring top float. We extrapolated the uppermost value to the surface with the same value. When there was complete ice cover at the mooring site the heat flux was set to zero. (We used a criterion of 85% ice concentration for this, but results are not sensitive to the precise choice).

As seen in Figure 9, the model does a reasonable job reproducing the depth of the observed mixed layer. There is significantly more scatter in the data, but this is to be expected based on the high degree of small-scale lateral variability that is present in regions of active convection (Pickart et al., 2002; Schott et al., 1996). Also, the model ignores lateral advection and hence any upstream preconditioning

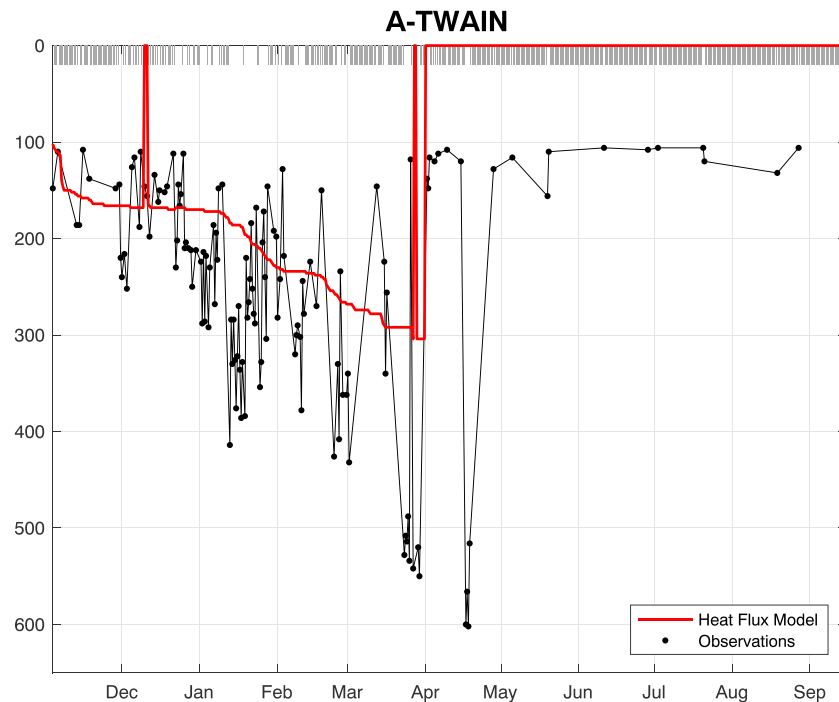


Figure 9. Simulated mixed-layer depth from the PWP model forced with the ERA-Interim heat flux time series (red line) for the A-TWAIN WHOI mooring, together with the observed mixed-layer depth at the Woods Hole Oceanographic Institution 1 site (black line and dots). Times with no mixed-layer depth are indicated by the gray lines at the top of the plot. A-TWAIN = long-term variability and trends in the Atlantic Water inflow region.

(although we note that the WHOI mooring site is outside of the core of the boundary current where the mean speed is only 7–8 cm/s; Figure 6); also, recall the good agreement in MLD between the WHOI mooring and the IOPAN site; Figure 9). From early-November until the time of 100% ice concentration in early-April, the model MLD deepens in a manner that corresponds to a low pass of the observations. Once full ice cover sets in and the heat flux goes to zero, the water column restratifies in accordance with the data (there are a small number of observed MLDs exceeding 100 m during this period). When the ice cover begins to decrease again and transitions to open water in late summer, the shortwave radiative heating dominates the turbulent heat flux and so the model continues to show no mixed layer, again consistent with the observations. The importance of local air-sea fluxes is in line with the results of Aagaard (1987) who, based on mooring measurements close to the A-TWAIN study area, concluded that changes in water mass properties are due more to vertical heat fluxes than lateral mixing. One-dimensional convection models forced by heat flux have also been used previously to shed light on the mixed layer characteristics north of Svalbard (Ivanov et al., 2016). In addition, Fer et al. (2017) used one-dimensional modeling to investigate the evolution of the hydrographic properties in the upper water column in this region between January and March. They found that vertical processes dominate as well, with a clear dependence on the eddy diffusivity.

The impact of the deepening mixed layer on the water column is seen clearly in the anomaly plots of Figure 10, where we have differenced the vertical profiles of temperature and salinity from their initial profiles, respectively (for each day we averaged the vertical traces from all of the profiling moorings). Also shown on the plot are the depth of the mixed layers (green dots) and the upper and lower bounds of the AW layer (black dots). This demonstrates how the AW layer becomes colder and fresher as it is ventilated locally via convective overturning. Note that, before the full ice cover sets in (in early April), the MLDs were occasionally approaching the depth of the lower boundary of the AW layer. That is, nearly the entire layer was being transformed. Note also that, after local convection ceased because of the ice cover, the part of the water column that was previously ventilated remained anomalously cold and fresh until the end of the record. This is likely due to the advection of transformed water from upstream.

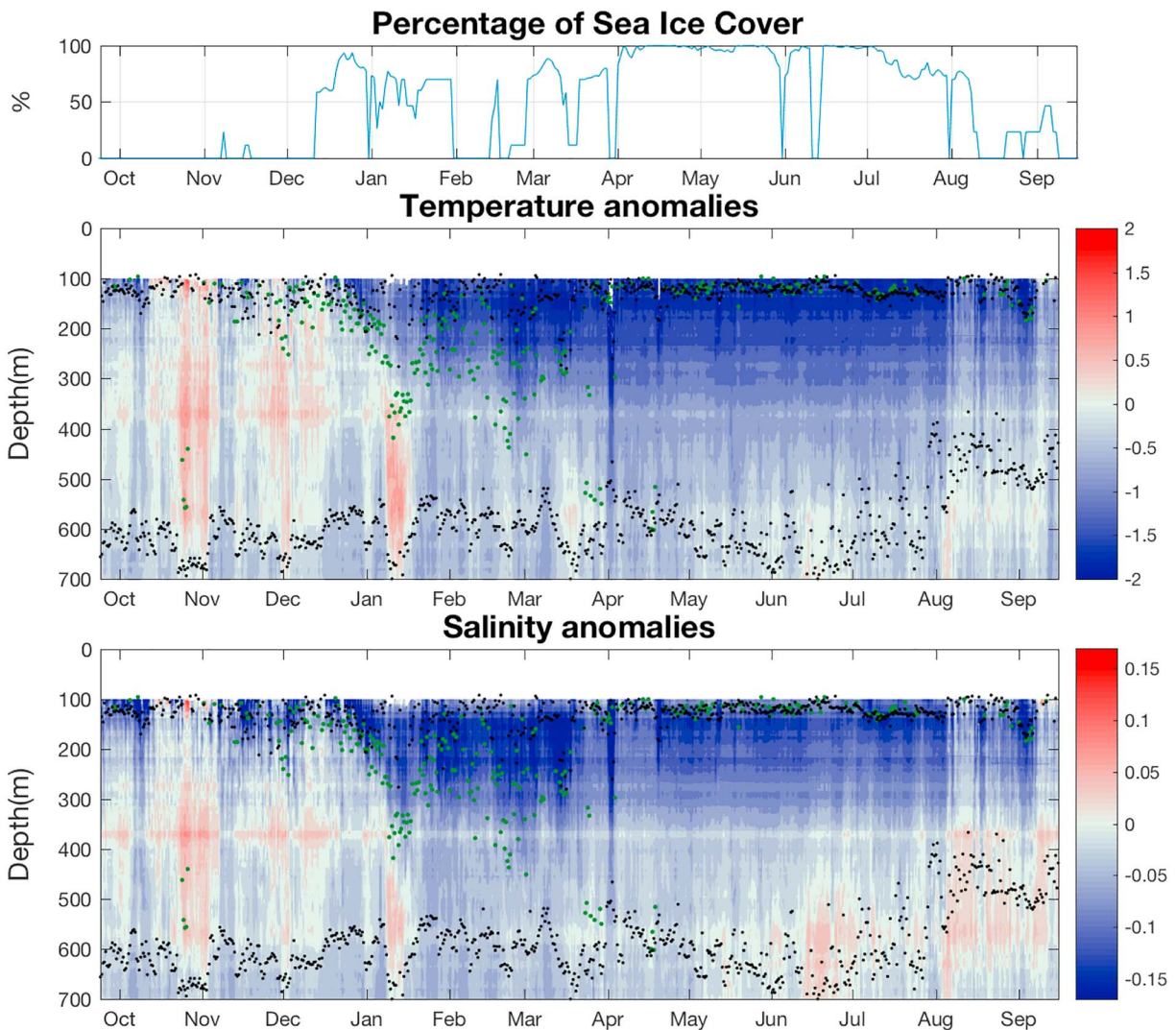


Figure 10. (a) Time series of percent sea ice coverage averaged over the long-term variability and trends in the Atlantic Water inflow region array. (b) Time-depth plot of potential temperature anomaly relative to the first profile. (c) Same as (b) except for salinity. The green dots indicate the mixed-layer depths, and the black dots denote the boundaries of the Atlantic Water layer. See the text for details. The signal at 360 m is due to the initial average profile, as it has a local minimum in temperature and salinity at that depth.

Figure 10 (as well as Figure 9) demonstrates that the ventilation of the AW layer was intermittent, and there were times when the mixed layer did not extend into the AW layer. In these instances, the top interface of the AW reappeared (i.e., the upper black dots in Figure 10). One can see that the water above the AW layer during these times was also becoming colder, fresher, and deeper as the season progressed, and some of these occurrences were associated with a sudden drop in sea ice concentration (melting of patches of sea ice advected over the array), for example, in late-December and mid-March.

To elucidate the effect of the ice cover on the mixed layers, we separated the MLD time series into three groups: full ice cover (concentrations greater than 85%), open water (concentrations less than 10%), and partial ice cover (concentrations between 10% and 85%). These are shown in Figure 11 for both the IOPAN site and the A-TWAIN site. It is clear that in highly consolidated ice the mixed layers were generally shallow (when present at all; the average MLD at the IOPAN and A-TWAIN sites are 71.2 and 163.9 m, respectively), due to the ice cover isolating the water column from the atmospheric forcing. The few deep MLDs that appeared were likely ventilated within leads. Conversely, the deepest mixed layers formed when there was little to no ice cover (average MLD 275.9 and 249.8 m at the IOPAN and A-TWAIN sites,

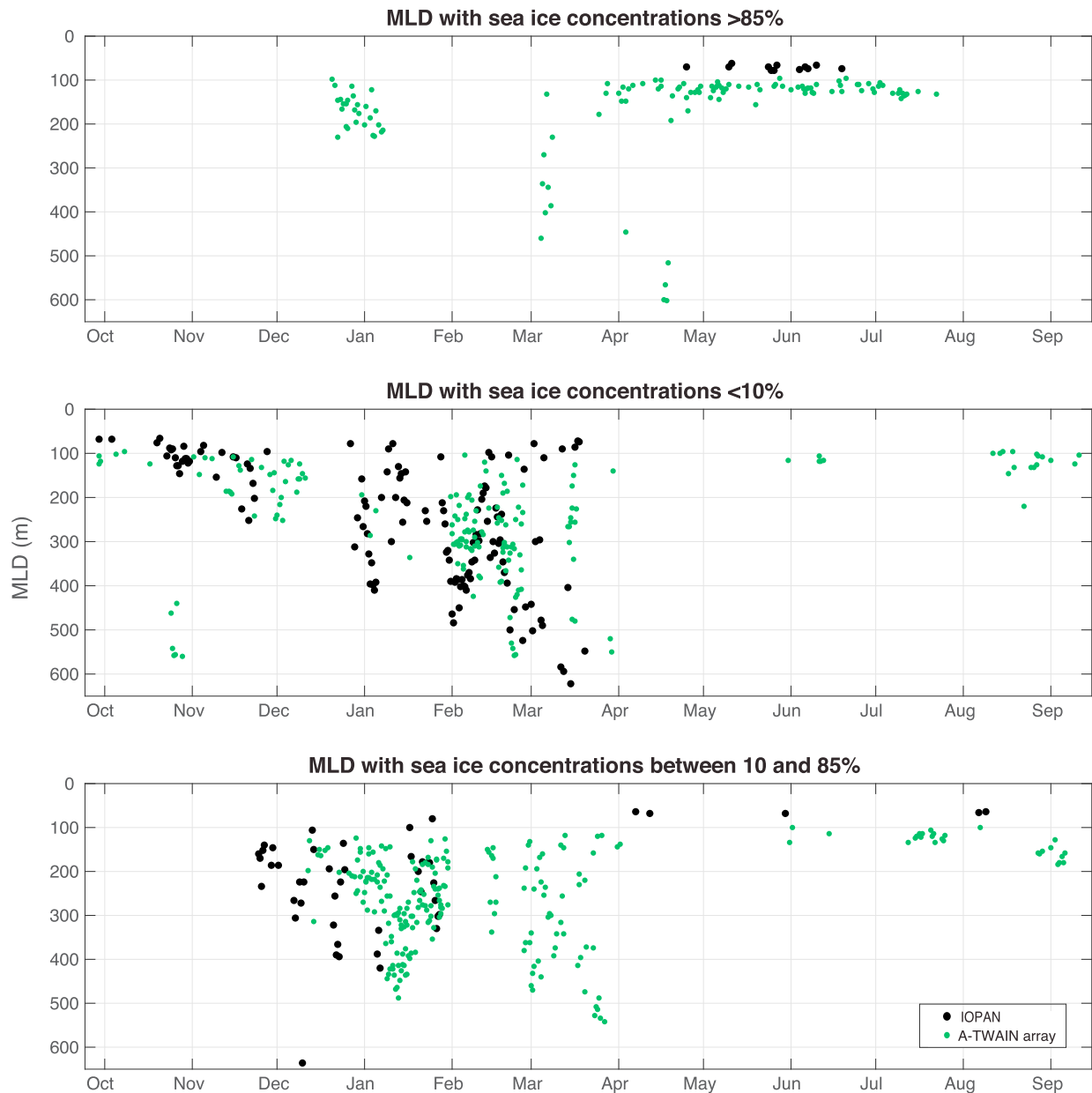


Figure 11. Time series of mixed-layer depth for the periods when the sea ice concentration is (a) greater than 85%, (b) less than 10%, and (c) between 10% and 85%, for the A-TWAIN array (green dots) and the upstream IOPAN mooring (black dots). IOPAN = Institute of Oceanology, Polish Academy of Sciences; A-TWAIN = Long-term variability and trends in the Atlantic Water inflow region; MLD = mixed-layer depth.

respectively). At the IOPAN site the MLD exceeded 600 m in mid-March. During periods of partial ice cover the MLDs were highly variable, ranging from very shallow to as deep as 400–500 m (average MLD 223.0 and 259.4 m at the IOPAN and A-TWAIN sites, respectively). Our results are consistent with Ivanov et al. (2016), who explored why the area north of Svalbard is ice free in winter (January–February). They found that summer ice decay allows a growing influence of oceanic heat capacity (on a seasonal scale) and more favorable conditions for upward heat release through convective overturning.

3.6. The AW Transformation

It is instructive to consider the evolution of the mixed layer throughout the year in T/S space, which is displayed in Figure 12a. As mentioned earlier in the paper, PSWw resides above the AW during part of the year.

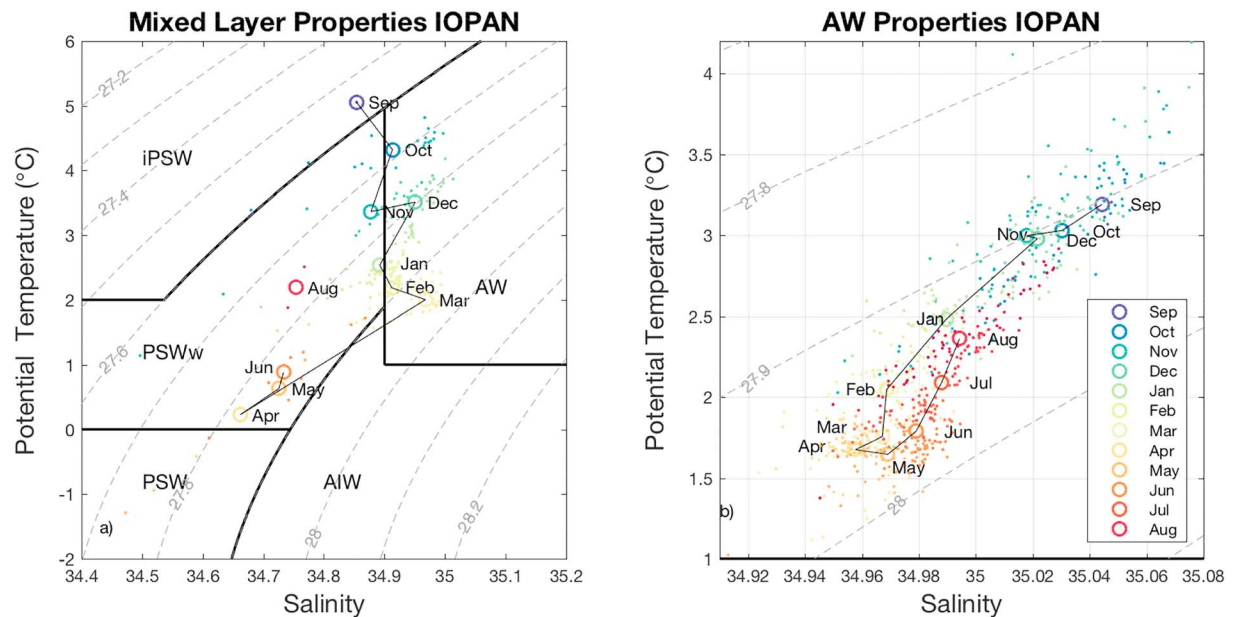


Figure 12. (a) Evolution of the average T/S of the mixed layer over the course of the year for the IOPAN mooring (see the legend). The circles denote the average value for each month (there is no mixed layer present during the month of July). The different water masses are as follows: PSW = polar surface water; iPSW = inshore polar surface water; PSWw = warm polar surface water; AW = Atlantic water; AIW = Arctic intermediate water. (b) Same as (a) except for the portion of the AW layer beneath the mixed-layer. Potential density contours are dashed.

Additionally, an early stage of this water mass (in late summer) has also been discussed in the literature, the so-called inshore Polar Surface Water (iPSW; Cokelet et al., 2008; Pérez-Hernández et al., 2017; Rudels et al., 2014). Using shipboard data, Pérez-Hernández et al. (2017) found iPSW to be centered around 50 m. For this reason, we use the data from the IOPOAN mooring whose profiles extend to 50 m (the WHOI MMPs only sampled to 100 m, and the NPI moorings did not have profilers).

One sees that the mixed layer is ventilating iPSW in September, but, soon after, the mixed layer penetrates the AW. From November to December the mixed layer remains relatively warm but becomes saltier. However, in mid-December, sea ice starts to appear on the surface which cools the surface layer (see Figure 10). This cold water subsequently induces deeper mixed layers until the end of March when the mixed layer is at its densest. Following the advent of near-complete ice cover at the end of March, the T/S character of the mixed layer changes abruptly since the layers are now quite shallow (Figures 8 and 10). At this point, for the remainder of the record, the mixed layer ventilates the PSWw, which becomes steadily warmer starting in April due to the lower contact with AW.

The T/S evolution of the part of the AW layer that is not locally ventilated at the IOPAN site is shown in Figure 12b. There is a steady progression of this part of the layer to colder temperatures and fresher salinities from the fall through the early-spring. These T/S changes did not compensate each other in density; hence, the lower part of the AW layer became denser. Then, starting in May, this nonlocally ventilated water became steadily warmer and saltier through the end of August, although it remained somewhat denser. The seasonal signal in salinity of this portion of the AW does not track the AW salinity in Fram Strait, suggesting that lateral mixing takes place along the boundary current.

4. Conclusions

A six-mooring array was deployed between September 2012 and September 2013 as part of the A-TWAIN project to characterize the Svalbard Branch of the AW boundary current. The data set has offered the most extensive view to date of this current over a full year. The vertical coverage of the moorings extended to 1,200-m depth, and, averaged over the year, the transport of the current over this depth range was 3.96 ± 0.32 Sv. The transport within the AW layer was 2.08 ± 0.24 Sv, which agrees relatively well with previous quasi-synoptic measurements from shipboard surveys (Pérez-Hernández et al., 2017; Våge et al., 2016).

The current was, for the most part, subsurface intensified, and its dominant variability was associated with pulsing rather than meandering.

Over the course of the measurement year there were three distinct seasonal periods. From August to mid-December the AW temperature, salinity, and transport were the highest; during this time, the region was relatively ice free. From mid-December to April the temperature and salinity decreased, reaching minimum values in February. Finally, from April to the end of July, the temperature and transport were generally the lowest of the year; during this period, the area was nearly fully ice covered. The AW transport of the Svalbard branch was 2.44 ± 0.12 Sv when the water was warmest and saltiest, decreasing to 1.10 ± 0.06 Sv when the water was coldest and freshest.

The seasonal cycle of AW temperature at the A-TWAIN site was significantly correlated with that in Fram Strait, with a 2-month lag. This is consistent with the estimated advective time between the two locations. A similar temperature seasonal cycle has been described in the area using single moorings (Ivanov et al., 2009; Randelhoff et al., 2015; Renner et al., 2018). In the Barents Sea, maximum temperatures are found 1 month earlier (September–October) than in our area (Lind & Ingvaldsen, 2012). Farther to the east, the maximum/minimum AW temperature occurs in winter to spring/summer, which suggests a further lag of several months with respect to the A-TWAIN region (Dmitrenko et al., 2006; Pnyushkov et al., 2015).

Deep mixed layers developed in the area from mid-October until April. At that point sea ice encroached the region from the north and the concentration approached 100%. This shielded the water column from the air-sea buoyancy flux, and consequently the mixed layers abruptly shallowed through meltwater input. The evolution of the MLD was well simulated using the one-dimensional PWP model forced with ERA-Interim reanalysis heat flux time series from the region. From late fall until early spring the mixed layers became progressively deeper, ventilating the AW layer. The maximum MLD exceeded 500 m before the onset of full ice cover in April. This is the first time that MLDs exceeding 150-m depth have been observed in the area. We suspect that the local freshening of the AW layer is the reason for the disagreement between the Fram Strait AW salinity signal and that recorded at the A-TWAIN site. These results suggest that as the ice cover continues to decrease in the southern Eurasian Basin, the AW layer will be more extensively modified via local ventilation. This will imply a lower heat and salinity flux throughout the Arctic basin and enhanced dense water formation.

Acknowledgments

We are grateful to the crew of the R/V *Lance* for the collection of the data. The U.S. component of A-TWAIN was funded by the National Science Foundation under grant ARC-1264098 as well as a grant from the Steven Grossman Family Foundation. The Norwegian component of A-TWAIN was funded by the “Arctic Ocean” flagship program at the Fram Centre. The data used in this study are available at <http://atwain.who.edu> and data.npolar.no (Sundfjord et al., 2017). The data from Fram Strait are available at <https://doi.pangaea.de/10.1594/PANGAEA.853902>

References

- Aagard, K., & Carmack, E. C. (1994). The Arctic Ocean and climate: A Perspective. In O. M. Johannessen, R. D. Muench, & J. E. Overland (Eds.), *The polar oceans and their role in shaping the global environment*, *Geophysical Monograph Series* (Vol. 85, pp. 5–20). Washington, DC: American Geophysical Union. <https://doi.org/10.1029/GM085p0005>
- Aagaard, K., Foldvik, A., & Hillman, S. R. (1987). The West Spitsbergen Current: Disposition and water mass transformation. *Journal of Geophysical Research*, *92*, 3778–3784.
- Bengtsson, L., Hodges, K. I., & Roeckner, E. (2006). Storm tracks and climate change. *Journal of Climate*, *19*, 3518–3543. <https://doi.org/10.1175/JCLI3815.1>
- Beszczynska-Möller, A., Fahrbach, E., Schauer, U., & Hansen, E. (2012). Variability in Atlantic water temperature and transport at the entrance to the Arctic Ocean, 1997–2010. *ICES Journal of Marine Science: Journal du Conseil*, *69*(5), 852–863.
- Cokelet, E. D., Tervalon, N., & Bellingham, J. G. (2008). Hydrography of the West Spitsbergen Current, Svalbard Branch: Autumn 2001. *Journal of Geophysical Research*, *113*, C01006. <https://doi.org/10.1029/2007JC004150>
- Crews, L., Sundfjord, A., Albretsen, J., & Hattermann, T. (2018). Mesoscale eddy activity and transport in the Atlantic water inflow region north of Svalbard. *Journal of Geophysical Research: Oceans*, *123*, 201–215. <https://doi.org/10.1002/2017JC013198>
- Dee, D. P., Uppala, S. M., Simmons, A. J., Berrisford, P., Poli, P., Kobayashi, S., et al. (2011). The ERA-interim reanalysis: Configuration and performance of the data assimilation system. *Quarterly Journal of the Royal Meteorological Society*, *137*(656), 553–597. <https://doi.org/10.1002/qj.828>
- Dmitrenko, I. A., Polyakov, I. V., & Kirillov, S. A. (2006). Seasonal variability of Atlantic water on the continental slope of the Laptev Sea during 2002–2004. *Earth and Planetary Science Letters*, *244*, 735–743. <https://doi.org/10.1016/j.epsl.2006.01.067>
- Dmitrenko, I. A., Rudels, B., Kirillov, S. A., Aksenov, Y. O., Lien, V. S., Ivanov, V. V., et al. (2015). Atlantic water flow into the Arctic Ocean through the St. Anna Trough in the northern Kara Sea. *Journal of Geophysical Research: Oceans*, *120*, 5158–5178. <https://doi.org/10.1002/2015JC010804>
- Fer, I., Peterson, A. K., Randelhoff, A., & Meyer, A. (2017). One-dimensional evolution of the upper water column in the Atlantic sector of the Arctic Ocean in winter. *Journal of Geophysical Research: Oceans*, *122*, 1665–1682. <https://doi.org/10.1002/2016JC012431>
- Fetterer, F., Stewart, J. S., & Meier W. N., (2015). MASAM2: Daily 4-km Arctic sea ice concentration, 2012–2014. Snow and Ice Data Center.
- Fratantoni, P. S., Pickart, R. S., Torres, D. J., & Scotti, A. (2001). Mean structure and dynamics of the shelfbreak jet in the Middle Atlantic Bight during fall and winter. *Journal of Physical Oceanography*, *31*(8), 2135–2156. [https://doi.org/10.1175/1520-0485\(2001\)031<2135:MSADOT>2.0.CO;2](https://doi.org/10.1175/1520-0485(2001)031<2135:MSADOT>2.0.CO;2)
- Hattermann, T., Isachsen, P. E., von Appen, W., Albretsen, J., & Sundfjord, A. (2016). Eddy-driven recirculation of Atlantic Water in Fram Strait. *Geophysical Research Letters*, *85*, 1259–1266. <https://doi.org/10.1002/2016GL06832>

- Håvik, L., Pickart, R. S., Våge, K., Torres, D., Thurnherr, A. M., Beszczynska-Möller, A., Walczowski, W., et al. (2017). Evolution of the East Greenland Current from Fram Strait to Denmark Strait: Synoptic measurements from summer 2012. *Journal of Geophysical Research: Oceans*, *122*, 1974–1994. <https://doi.org/10.1002/2016JC012228>
- Ivanov, V., Alexeev, V., Koldunov, N. V., Repina, I., Sandø, A. B., Smedsrud, L. H., & Smirnov, A. (2016). Arctic Ocean heat impact on regional ice decay: A suggested positive feedback. *Journal of Physical Oceanography*, *46*(5), 1437–1456. <https://doi.org/10.1175/JPO-D-15-0144.1>
- Ivanov, V. V., Polyakov, I. V., Dmitrenko, I. A., Hansen, E., Repina, I. A., Kirillov, S. A., et al. (2009). Seasonal variability in Atlantic Water off Spitsbergen. *Deep Sea Research Part I: Oceanographic Research Papers*, *56*(1), 1–14. <https://doi.org/10.1016/j.dsr.2008.07.013>
- Koenig, Z., Provost, C., Sennéchaël, N., Garric, G., & Gascard, J.-C. (2017). The Yermak pass branch: A major pathway for the Atlantic water north of Svalbard? *Journal of Geophysical Research: Oceans*, *122*, 9332–9349. <https://doi.org/10.1002/2017JC013271>
- Koenig, Z., Provost, C., Villaceros Robineau, N., Sennéchaël, N., Meyer, A., Lellouche, J. M., & Garric, G. (2017). Atlantic waters inflow north of Svalbard: Insights from IAOOS observations and Mercator Ocean global operational system during N-ICE2015. *Journal of Geophysical Research: Oceans*, *122*, 1254–1273. <https://doi.org/10.1002/2016JC012424>
- Kolås, E., & Fer, I. (2018). Hydrography, transport and mixing of the West Spitsbergen Current: The Svalbard Branch in summer 2015. *Ocean Science*, *14*, 1603–1618. [ocean-sci-discuss.net. https://doi.org/10.5194/os-2018-86](https://doi.org/10.5194/os-2018-86)
- Lind, S., & Ingvaldsen, R. B. (2012). Variability and impacts of Atlantic Water entering the Barents Sea from the north. *Deep Sea Research Part I: Oceanographic Research Papers*, *62*, 70–88. <https://doi.org/10.1016/j.dsr.2011.12.007>
- Meyer, A., Fer, I., Sundfjord, A., & Peterson, A. K. (2017). Mixing rates and vertical heat fluxes north of Svalbard from Arctic winter to spring. *Journal of Geophysical Research: Oceans*, *122*, 4569–4586. <https://doi.org/10.1002/2016JC012441>
- Meyer, A., Sundfjord, A., Fer, I., Provost, C., Villaceros Robineau, N., Koenig, Z., et al. (2017). Winter to summer oceanographic observations in the Arctic Ocean north of Svalbard. *Journal of Geophysical Research: Oceans*, *122*, 6218–6237. <https://doi.org/10.1002/2016JC012391>
- Nurser, A. J. G., & Bacon, S. (2014). The Rossby radius in the Arctic Ocean. *Ocean Science*, *10*(6), 967–975. <https://doi.org/10.5194/os-10-967-2014>
- Onarheim, I. H., Smedsrud, L. H., Ingvaldsen, R. B., & Nilsen, F. (2014). Loss of sea ice during winter north of Svalbard. *Tellus A*, *66*(1). <https://doi.org/10.3402/tellusa.v66.23933>
- Pérez-Hernández, M. D., Pickart, R. S., Pavlov, V., Våge, K., Ingvaldsen, R., Sundfjord, A., et al. (2017). The Atlantic Water boundary current north of Svalbard in late summer. *Journal of Geophysical Research: Oceans*, *122*, 2269–2290. <https://doi.org/10.1002/2016JC012486>
- Pickart, R. S., Torres, D. J., & Clarke, R. A. (2002). Hydrography of the Labrador Sea during active convection. *Journal of Physical Oceanography*, *32*(2), 428–457. [https://doi.org/10.1175/1520-0485\(2002\)032<0428:HOTLSD>2.0.CO;2](https://doi.org/10.1175/1520-0485(2002)032<0428:HOTLSD>2.0.CO;2)
- Pnyushkov, A. V., Polyakov, I., Rember, R., Alkire, M. B., Ashik, I. M., Bauman, T. M., et al. (2018). Heat, salt, and volume transports in the eastern Eurasian Basin of the Arctic Ocean, from two years of mooring observations. *Ocean Science*, *14*, 1349–1371. [ocean-sci-discuss.net](https://doi.org/10.5194/os-2018-86)
- Pnyushkov, A. V., Polyakov, I. V., Ivanov, V. V., Aksenov, Y., Coward, A. C., Janout, M., & Rabe, B. (2015). Structure and variability of the boundary current in the Eurasian Basin of the Arctic Ocean. *Deep Sea Research Part I: Oceanographic Research Papers*, *101*, 80–97. <https://doi.org/10.1016/j.dsr.2015.03.001>
- Polyakov, I. V., Alexeev, V. A., Ashik, I. M., Bacon, S., Beszczynska-Möller, A., Carmack, E. C., et al. (2011). Fate of early 2000s Arctic warm water pulse. *Bulletin of the American Meteorological Society*, *92*(5), 561–566. <https://doi.org/10.1175/2010BAMS2921.1>
- Price, J. F., Weller, R. A., & Pinkel, R. (1986). Diurnal cycling—Observations and models of the upper ocean response to diurnal heating, cooling, and wind mixing. *Journal of Geophysical Research*, *91*(C7), 8411–8427. <https://doi.org/10.1029/JC091iC07p08411>
- Randelhoff, A., Sundfjord, A., & Reigstad, M. (2015). Seasonal variability and fluxes of nitrate in the surface waters over the Arctic shelf slope. *Geophysical Research Letters*, *42*, 3442–3449. <https://doi.org/10.1002/2015GL063655>
- Renner, A. H. H., Sundfjord, A., Janout, M. A., Ingvaldsen, R. B., Möller, A. B., Pickart, R. S., et al. (2018). Variability and redistribution of heat in the Atlantic water boundary current north of Svalbard. *Journal of Geophysical Research: Oceans*, *123*, 6373–6391. <https://doi.org/10.1029/2018JC013814>
- Rudels, B. (2013). Arctic ocean circulation, processes and water masses: A description of observations and ideas with focus on the period prior to the international polar year 2007-2009. *Progress in Oceanography*, *132*, 22–67. <https://doi.org/10.1016/j.pocean.2013.11.006>
- Rudels, B., Jones, E. P., Anderson, L. G., & Kattner, G. (2013). On the intermediate depth waters of the Arctic Ocean. In O. M. Johannessen, R. D. Muench, & J. E. Overland (Eds.), *The polar oceans and their role in shaping the global environment*. <https://doi.org/10.1029/GM085p0033>
- Rudels, B., Korhonen, M., Schauer, U., Pisarev, S., Rabe, B., & Wisotzki, A. (2014). Circulation and transformation of Atlantic water in the Eurasian Basin and the contribution of the Fram Strait inflow branch to the Arctic Ocean heat budget. *Progress in Oceanography*, *132*, 128–152.
- Schauer, U., Fahrbach, E., Østerhus, S., & Rohardt, G. (2004). Arctic warming through the Fram Strait: Oceanic heat transport from 3 years of measurements. *Journal of Geophysical Research*, *109*, C06026. <https://doi.org/10.1029/2003JC001823>
- Schauer, U., Muench, R. D., Rudels, B., & Timokhov, L. (1997). Impact of eastern Arctic shelf waters on the Nansen Basin intermediate layers. *Journal of Geophysical Research*, *102*, 3371–3382.
- Schauer, U., Rudels, B., Jones, E. P., Anderson, L. G., Muench, R. D., Björk, G., et al. (2002). Confluence and redistribution of Atlantic water in the Nansen, Amundsen and Makarov basins. *Annales Geophysicae*, *20*(2), 257–273. <https://doi.org/10.5194/angeo-20-257-2002>
- Schott, F., Visbeck, M., Send, U., Fischer, J., Stramma, L., & Desaubies, Y. (1996). Observations of deep convection in the Gulf of Lions, Northern Mediterranean, during the winter of 1991/92. *Journal of Physical Oceanography*, *26*(4), 505–524. [https://doi.org/10.1175/1520-0485\(1996\)026<0505:OODCIT>2.0.CO;2](https://doi.org/10.1175/1520-0485(1996)026<0505:OODCIT>2.0.CO;2)
- Sundfjord, A., Renner, A. H. H., & Beszczynska-Möller, A. (2017). A-TWAIN mooring hydrography and current data Sep 2012 - Sep 2013 [Data set]. <https://doi.org/10.21334/npolar.2017.73d0ea3a>
- Våge, K., Pickart, R. S., Pavlov, V., Lin, P., Torres, D. J., Ingvaldsen, R., et al. (2016). The Atlantic Water boundary current in the Nansen Basin: Transport and mechanisms of lateral exchange. *Journal of Geophysical Research: Oceans*, *121*, 6946–6960. <https://doi.org/10.1002/2016JC011715>
- von Appen, W. J., A. Beszczynska-Möller, & E. Fahrbach (2015). Physical oceanography and current meter data from mooring F3-15. Pangea, doi: <https://doi.org/10.1594/PANGAEA.853902>
- von Appen, W. J., Schauer, U., Hattermann, T., & Beszczynska-Möller, A. (2016). Seasonal cycle of mesoscale instability of the West Spitsbergen Current. *Journal of Physical Oceanography*, *46*(4), 1231–1254. <https://doi.org/10.1175/JPO-D-15-0184.1>
- Zhao, M., Timmermans, M. L., Cole, S., Krishfield, R., Proshutinsky, A., & Toole, J. (2014). Characterizing the eddy field in the Arctic Ocean halocline. *Journal of Geophysical Research: Oceans*, *119*, 8800–8817. <https://doi.org/10.1002/2014JC010488>